International Journal of Pavement Engineering

ISSN: (Print) (Online) Journal homepage: https://www.tandfonline.com/loi/gpav20

Evolution characteristics of crack and energy of low-grade highway under impact load

Qindong Lin, Chun Feng, Xinguang Zhu, Genghao Zhang & Shihai Li

To cite this article: Qindong Lin, Chun Feng, Xinguang Zhu, Genghao Zhang & Shihai Li (2021): Evolution characteristics of crack and energy of low-grade highway under impact load, International Journal of Pavement Engineering, DOI: 10.1080/10298436.2021.1886294

To link to this article: https://doi.org/10.1080/10298436.2021.1886294

INTERNATIONAL JOURNAL OF PAVEMENT ENGINEERING
https://doi.org/10.1080/10298436.2021.1886294

Taylor & Francis
Taylor & Francis Group

Evolution characteristics of crack and energy of low-grade highway under impact load

Qindong Lin[a,b], Chun Feng[a], Xinguang Zhu[a,b], Genghao Zhang[a,b] and Shihai Li[a,b]

[a]Key Laboratory for Mechanics in Fluid Solid Coupling Systems, Institute of Mechanics, Chinese Academy of Sciences, Beijing, People's Republic of China; [b]School of Engineering Science, University of Chinese Academy of Sciences, Beijing, People's Republic of China

ABSTRACT

To analyse the feasibility of the low-grade highway as a launch site in military applications and improve the pavement crushing technology in civilian applications, this study investigates the evolution characteristics of a low-grade highway under impact load, including deflection, crack, and energy, via the continuum–discontinuum element method (CDEM). To this end, this paper proposes an energy statistics algorithm, and the correctness is verified. Then, a quarter three-dimensional numerical model of an asphalt concrete highway is established, and the effectiveness of CDEM in simulating the deflection of the highway under impact load is validated. Finally, an existing asphalt concrete highway structure is selected to study the evolution characteristics via numerical simulation. The results demonstrate the consistency between the variations of deflection at the load centre and the impact load. The deflection is primarily caused by the compressive deformation of subgrade. Crack planes mainly occur when the impact load increases rapidly. The variation of various constituent energies is different but closely related to the change in impact load.

ARTICLE HISTORY
Received 6 March 2020
Accepted 1 February 2021

KEYWORDS
Impact load; low-grade highway; evolution characteristic of deflection; evolution characteristic of crack; evolution characteristic of energy

1. Introduction

Highways play a pivotal role in civilian applications (e.g. logistics, personnel mobility, etc.) (Jha *et al.* 2012, Holl and Mariotti 2018, Zhang *et al.* 2020b). Highways have also drawn the interest of defense research because of their unique advantages in military applications (e.g. missile launching, aircraft landing, etc.) (Wei *et al.* 2017). According to the U.S. Department of Defense and the U.S. Federal Aviation Administration, loads of slow-moving/static aircraft on pavements are more significant than those of rapidly moving aircraft, because the lift force generated by the latter counteracts a portion of its weight. However, during missile launch, the load applied to the highways is the impact load, which has a short duration and a large amplitude (Ren *et al.* 2014, Zhou *et al.* 2014, Huang *et al.* 2017). In addition, with the rapid development of pavement crushing technology in the civilian applications, some machines (e.g. the multi-head breaker, impact roller crushing, etc.) are widely used. The load exerted on pavements by these machines can be simplified to an impact load (Ceylan *et al.* 2008, Ge *et al.* 2015, Liu *et al.* 2019). Since the majority of highways are low-grade highways, studying the mechanical response of these highways under impact load is of great significance to both civilian and military applications.

The current methods for studying the mechanical response of highways mainly include theoretical analysis, field experiments, and numerical simulation. Highways are composed of pavement and subgrade. Pavements are roughly classified into two types: rigid pavement and flexible pavement. The stress analysis and design approaches involving rigid pavements are mainly based on a thin slab on an elastic foundation. Westergaard modelled the pavement as a homogenous, isotropic, and elastic thin slab resting on a Winkler foundation and proposed a complete theory of structural behaviour of pavement (Westergaard 1926, 1933, 1939, 1948). Existing methods of flexible pavement design are primarily based on the structural analysis of layered systems. For the subgrade, the layered system is idealised as a Winkler foundation model, a Kelvin foundation model, or a Pasternak foundation model. The beam–foundation system can be used as an idealisation of the interaction between the pavement and subgrade. The pavement can be simplified as a Rayleigh, Timoshenko, or Euler–Bernoulli beam (Timoshenko 1921, 1922, Luo *et al.* 2015, Szyłko-Bigus *et al.* 2019, Ebrahimi-Mamaghani *et al.* 2020, Zhen *et al.* 2020).

Researchers have also studied the mechanical response of highways under impact loads based on theoretical analysis. To study the correlation between deflection and distance from the load centre, Liang and Zeng (2002), Alisjahbana *et al.* (2018), and Zhao and Jiang (2018) proposed that the dynamic deflection decreases with increasing distance, and that the variation trend of the deflection time-history curve with varying distance is consistent. Based on the spectral element method, Gu *et al.* (2014) found that, although the deflection of pavement under an FWD pulse load decreases with increasing depth, the variation trend of the deflection time-history curve remains consistent. To understand the influence of the interface condition and isotropy on the mechanical response of highways, Liu *et al.* (2018) theorised an obvious discontinuity in the radial stress at the location of the sliding interface, while You *et al.* (2018) proposed that

CONTACT Chun Feng fengchun@imech.ac.cn

the displacement calculated using isotropic solutions was quite different from transversely isotropic solutions.

Field experiments are another important research method. Several researchers (Zhang *et al.* 2017, Iqbal *et al.* 2019) studied the influence of drop height and found that the punching effect became more pronounced with increasing drop height and that the initial and final impact strengths decreased exponentially. Picoux *et al.* (2009) studied the correlation between deflection and distance from the load centre based on field experiments. They found that the time-history curves of impact load and deflection were consistent, and that deflection decreased with increasing distance.

Because theoretical analysis and field experiment often omit a few influencing factors for simplification, researchers have studied the mechanical response of highways based on numerical simulation to include those factors. For example, Sun and Duan (2013) studied the influence of factors based on ABAQUS, such as vehicle speed, crack location, crack depth, and damping ratio on the dynamic response of highways. Assogba *et al.* (2020) simulated the crushing and cracking processes of concrete pavement under a multi-head impact load and they found that tensile crack planes mainly propagated along the long axis of rectangular hammerheads. With the widespread use of missile unsupported launch (Zhao and Jiang 2018), researchers have studied the dynamic response of highways during the missile launch. Huang *et al.* (2017) found that the maximum displacement is at the load centre of the launch area. Zhang *et al.* (2015) found that the degree of damage to the surface course increased rapidly in a short time, before becoming constant after a certain value. In addition, damage to the central part is more severe than that to the surrounding area. Zhou *et al.* (2014) found that the deflection time-history curve below the canister launcher was closely related to its load time-history curve.

Currently, numerical simulation of the mechanical response of a highway under impact load has two main disadvantages. First, the simulation is primarily based on the elastic–plastic finite element method and the viscoelastic–plastic finite element method. These methods are based on continuum mechanics, which makes it is difficult to simulate the process of crack generation, propagation, and complex contact under impact load. Second, for the mechanical response, few mechanical quantities (i.e. deflection and stress) have drawn attention. However, the evolution characteristics of cracks and energy under impact loads have rarely been studied.

This study investigates the evolution characteristics of deflection, crack, and energy of a low-grade asphalt concrete highway under impact load using the continuum–discontinuum element method (CDEM). The remainder of this paper is structured as follows. In Section 2, the basic concept of CDEM is explained, and an energy statistics algorithm is proposed. In Section 3, a quarter three-dimensional numerical model of a low-grade asphalt concrete highway is established, and the effectiveness of the CDEM in simulating the deflection of a highway under an impact load is validated. In Section 4, the mechanical response of a low-grade asphalt concrete highway under impact load is simulated by CDEM, and the evolution characteristics of deflection, crack, and energy are analysed in detail. The main findings of the study are summarised in Section 5.

2. Methodology

2.1. Algorithm description of CDEM

2.1.1. Basic concept

The CDEM is a dynamic explicit algorithm that simulates the entire process of material failure from continuous deformation to crack and movement. The numerical model of the CDEM is composed of a block and an interface (Figure 1). A block consists of one or more elements, and it is used to characterise the continuous features (e.g. elasticity, plasticity, etc.) of the material. The common boundary between two blocks is called the interface, and it is used to characterise discontinuous features such as crack and slip. The interface includes the real interface (the black solid lines in Figure 1(a)) and the virtual interface (the red dotted lines in Figure 1(a)). The real interface is used to characterise the real discontinuous features of the material. The virtual interface has two main purposes: to connect two blocks and transfer mechanical information; and to provide potential space for crack generation and propagation. CDEM introduces a contact model that combines a semi-spring and a semi-edge at the interface to accurately calculate contact force and failure state between blocks (the green line BB′, JJ′, and KK′ in Figure 1(c)).

CDEM establishes a governing equation through the Lagrange energy system, which can be expressed as

$$\boldsymbol{M}\boldsymbol{a}(t) + \boldsymbol{C}\boldsymbol{v}(t) + \boldsymbol{K}\boldsymbol{u}(t) = \boldsymbol{F}(t) \tag{1}$$

where $\boldsymbol{a}(t)$, $\boldsymbol{v}(t)$, and $\boldsymbol{u}(t)$ denote the acceleration vector, velocity vector, and displacement vector, respectively. $\boldsymbol{M}$, $\boldsymbol{C}$, and $\boldsymbol{K}$ denote the mass, damping, and stiffness matrices, respectively. $\boldsymbol{F}(t)$ is the vector of the external force.

2.1.2. Constitutive model

The viscosity of asphalt concrete is usually considered in relevant high-temperature applications. Because this study investigated the dynamic responses of asphalt concrete pavement under a second-time load at normal temperature, the viscosity of asphalt concrete was neglected. That is, the viscosity term was not included in the current constitutive model. The Mohr–Coulomb model was selected as the element constitutive model. The principal stresses σ_1, σ_2, and σ_3 were calculated based on the stress tensor $\boldsymbol{\sigma_{ij}}$. The relations in Equation (2) were used to determine whether the element met the Mohr–Coulomb and maximum tensile stress criteria.

$$\begin{cases} f_s = \sigma_1 - \sigma_3 N_\varphi + 2c_e\sqrt{N_\varphi} \\ f_t = \sigma_3 - \sigma_{et} \\ h = f_t + \alpha_P(\sigma_1 - \sigma_P) \end{cases} \tag{2}$$

where c_e denotes the element cohesion strength, and σ_{et} denotes the element tensile strength. N_φ, α_P, and σ_P are constants, and they are expressed as

$$\left.\begin{aligned} N_\varphi &= \frac{1+\sin\varphi_e}{1-\sin\varphi_e} \\ \alpha_P &= \sqrt{1+N_\varphi^2} + N_\varphi \\ \sigma_P &= \sigma_t N_\varphi - 2c\sqrt{N_\varphi} \end{aligned}\right\} \tag{3}$$

where φ_e is the element friction angle.

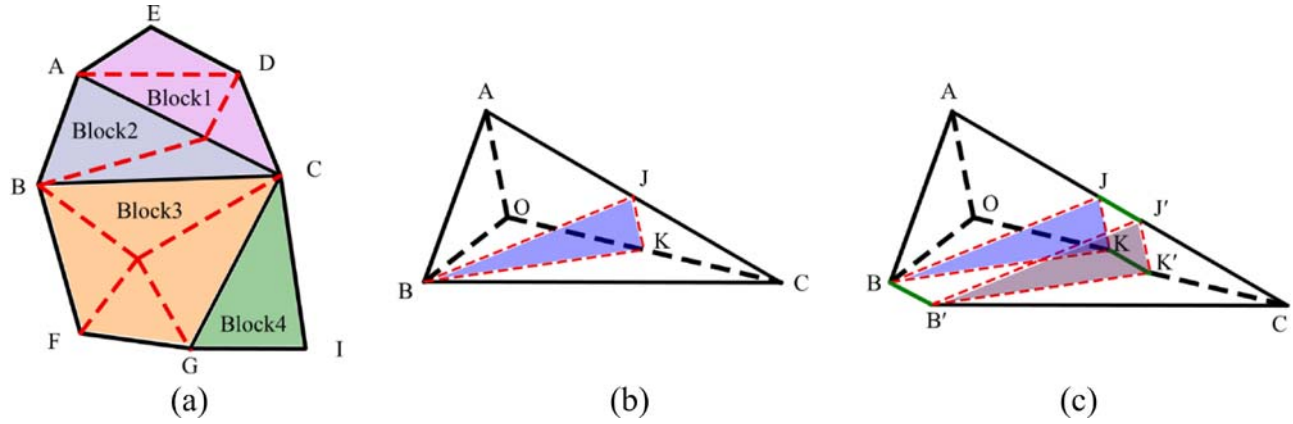

Figure 1. Schematic diagram of block and interface in the CDEM.

If $f_s \geq 0$ and $h \leq 0$, shear failure will occur. If $f_t \geq 0$ and $h > 0$, tensile failure will occur.

The CDEM introduces a contact model that combines a semi-spring and a semi-edge at the interface to accurately calculate the contact force and failure state (Feng *et al.*, 2014). The Mohr–Coulomb fracture criterion (Equation (4)) and maximum tensile stress criterion (Equation (5)) were applied to the interface.

$$\begin{cases} \text{if } F_s \geq F_n \tan\varphi + c_p s \\ F_s = F_n \tan\varphi + c_p s \\ \text{next step } c_{\mathrm{p}} = 0,\ \ \sigma_{\mathrm{pt}} = 0 \end{cases} \tag{4}$$

$$\begin{cases} \text{if } -F_n \geq \sigma_{\mathrm{pt}} s \\ F_n = F_s = 0 \\ \text{next step } c_p = 0,\ \ \sigma_{\mathrm{pt}} = 0 \end{cases} \tag{5}$$

where σ_{pt} denotes the spring tensile strength, c_p denotes the spring cohesive strength, φ denotes the spring friction angle, and s is the spring contact area.

To quantitatively characterise the interface failure state, crack ratio α_{D} is proposed, which is a dimensionless value.

$$\alpha_{\mathrm{D}} = \frac{S_c}{S_a} \tag{6}$$

where S_c is the area of the fracture interface, and S_a is the area of all interfaces. The value range of α_{D} is [0,1].

2.2. Energy statistics algorithm

2.2.1. Element deformation energy W_{EE}

The element deformation energy W_{EE} includes the elastic deformation energy and plastic deformation energy. First, the elastic deformation energy density w_{ee} and plastic deformation energy density w_{ep} were obtained based on the stress tensor $\boldsymbol{\sigma}_{\mathbf{ij}}$, elastic strain component $\boldsymbol{\varepsilon}_{\mathbf{eij}}$, and plastic strain component $\boldsymbol{\varepsilon}_{\mathbf{pij}}$ (Equations (7) and (8)). Subsequently, the deformation energy of each element was calculated. Finally, the cumulative deformation energy value W_{EE} of all elements was obtained (Equation (9)).

$$w_{\mathrm{ee}} = 0.5\varepsilon_{\mathrm{eij}}\sigma_{\mathrm{ij}} \tag{7}$$

$$w_{\mathrm{ep}} = \varepsilon_{\mathrm{pij}}\sigma_{\mathrm{ij}} \tag{8}$$

$$W_{\mathrm{EE}} = \sum_{k=1}^{N_{\mathrm{E}}} V_{\mathrm{k}}(w_{\mathrm{ee}} + w_{\mathrm{ep}}) \tag{9}$$

where V_{k} denotes the element volume, and N_{E} is the number of elements.

2.2.2. Element kinetic energy W_{EV}

First, the element centroid velocity was calculated from the node velocity (Equation (10)). Subsequently, the kinetic energy of each element was calculated. Finally, the cumulative kinetic energy value W_{EV} of all elements was obtained (Equation (11)).

$$\begin{cases} v_{\mathrm{ex}} = \dfrac{1}{n_{\mathrm{o}}}\displaystyle\sum_{i=1}^{n_{\mathrm{o}}} v_{\mathrm{ox}}^{\mathrm{i}} \\ v_{\mathrm{ey}} = \dfrac{1}{n_{\mathrm{o}}}\displaystyle\sum_{i=1}^{n_{\mathrm{o}}} v_{\mathrm{oy}}^{\mathrm{i}} \\ v_{\mathrm{ez}} = \dfrac{1}{n_{\mathrm{o}}}\displaystyle\sum_{i=1}^{n_{\mathrm{o}}} v_{\mathrm{oz}}^{\mathrm{i}} \end{cases} \tag{10}$$

$$W_{\mathrm{EV}} = \sum_{k=1}^{N_{\mathrm{E}}} \frac{1}{2} m_{\mathrm{k}}(v_{\mathrm{ex}}^2 + v_{\mathrm{ey}}^2 + v_{\mathrm{ez}}^2) \tag{11}$$

where $v_{\mathrm{ox}}^{\mathrm{i}}$ $v_{\mathrm{oy}}^{\mathrm{i}}$ and $v_{\mathrm{oz}}^{\mathrm{i}}$ are the components of the i-th node velocity along the X, Y, and Z directions, respectively. n_{o} denotes the number of nodes. v_{ex}, v_{ey}, and v_{ez} denote the components of the element centroid velocity along the X, Y, and Z directions.

2.2.3. Spring deformation energy W_{PE}

The numerical springs at the interface can transfer tensile, compressive, and shear forces. In the local coordinate system, the spring force was decomposed into F_{px}, F_{py}, and F_{pz}. F_{pz} is the normal force, and F_{px} and F_{py} are the tangential forces. The deformation energy of each spring was calculated, followed by the cumulative deformation energy value W_{PE} of all springs

(Equation (12)).

$$W_{\mathrm{PE}} = \sum_{k=1}^{N_{\mathrm{P}}} \left(\frac{1}{2}\frac{F_{\mathrm{pz}}^2}{k_n} + \frac{1}{2}\frac{F_{\mathrm{px}}^2}{k_s} + \frac{1}{2}\frac{F_{\mathrm{py}}^2}{k_s}\right) \tag{12}$$

where N_p is the number of springs, *and* k_n and k_s denote the spring normal stiffness and spring tangential stiffness, respectively.

2.2.4. Spring fracture energy W_{PC}

When the spring undergoes tensile failure, the tensile strength σ_{pt} and cohesive strength c_{p} are reduced to 0. Hence, the fracture energy should include the tensile fracture energy w_{pt} and shear fracture energy w_{ps}. When the spring undergoes shear failure, the cohesive strength c_{p} and tensile strength σ_{pt} are reduced to 0. Since the spring is in compression, the fracture energy will only include the shear fracture energy w_{ps}.

First, the fracture energy w_{pc} of each broken spring was calculated according to the failure type (Equation (15)). Then, the cumulative fracture energy W_{PC} of all broken springs was obtained (Equation (16)).

$$w_{\mathrm{pt}} = \frac{1}{2}\frac{(\sigma_{\mathrm{pt}} s)^2}{k_n} \tag{13}$$

$$w_{ps} = \frac{1}{2}\frac{(c_{\mathrm{p}} s)^2}{k_{\mathrm{s}}} + F_{\mathrm{pz}} \tan\varphi \frac{c_{\mathrm{p}} s}{k_{\mathrm{s}}} \tag{14}$$

$$w_{\mathrm{pc}} = \begin{cases} w_{\mathrm{pt}} + w_{\mathrm{ps}} & \text{if Tensile failure} \\ w_{\mathrm{ps}} & \text{if Shear failure} \end{cases} \tag{15}$$

$$W_{\mathrm{PC}} = \sum_{k=1}^{N_{\mathrm{PC}}} w_{\mathrm{pc}} \tag{16}$$

where N_{PC} represents the number of broken springs, σ_{pt} denotes the spring tensile strength, s denotes the spring contact area, c_{p} denotes the spring cohesion strength, and φ denotes the spring friction angle.

2.2.5. Friction energy W_R

After the interface breaks, the surfaces of elements from both sides in contact move relative to each other and expend energy. This friction energy is determined by the tangential forces F_{pi} (i.e. F_{px} and F_{py}) and the relative tangential displacements ΔU_{i} (i.e. ΔU_{x} and ΔU_{y}). From time t–Δt to time t, the relative tangential displacement is closely related to the spring state and elongation. ΔU_{i} is expressed as:

$$\Delta U_i = \begin{cases} 0 & \text{if } \mathrm{G}_{t\text{-}\Delta t} = \text{unbroken and } \mathrm{G}_t = \text{unbroken} \\ (U_i^t - \frac{F_{\mathrm{pi}}^t}{k_{\mathrm{s}}}) - (U_{\mathrm{i}}^{t-\Delta t} - \frac{F_{\mathrm{pi}}^{t-\Delta t}}{k_{\mathrm{s}}}) & \text{if } \mathrm{G}_{t\text{-}\Delta t} = \text{unbroken and } \mathrm{G}_t = \text{broken} \\ (U_i^t - \frac{F_{\mathrm{pi}}^t}{k_s}) - (U_i^{t-\Delta t} - \frac{F_{\mathrm{pi}}^{t-\Delta t}}{k_{\mathrm{s}}}) & \text{if } \mathrm{G}_{t\text{-}\Delta t} = \text{broken and } \mathrm{G}_t = \text{broken} \\ 0 & \text{if } \mathrm{G}_{t\text{-}\Delta t} = \text{broken and } \mathrm{G}_t = \text{unbroken} \end{cases} \tag{17}$$

where $U_i^{t-\Delta t}$ denotes the elongation component at time t–Δt, U_i^t denotes the elongation component at time t, $F_{\mathrm{pi}}^{t-\Delta t}$ denotes the tangential force component at time t–Δt, F_{pi}^t denotes the tangential force component at time t, $G_{t-\Delta t}$ and G_t denote the spring state at time t–Δt and time t, respectively.

The expression of W_{R} is written as:

$$W_{\mathrm{R}} = \sum_{k=1}^{N_{\mathrm{P}}} (F_{px}\Delta U_{\mathrm{x}} + F_{py}\Delta U_{\mathrm{y}}) \tag{18}$$

2.2.6. Damping energy W_D

Local damping was adopted for the numerical calculation. The correspondence between the critical damping ratio ξ and the local damping coefficient c_{d} is $\xi = \pi c_{\mathrm{d}}$. First, the energy consumed by local damping at each node was calculated. Then, the cumulative damping energy value W_{D} of all nodes was obtained. The expression is written as

$$W_{\mathrm{D}} = \sum_{k=1}^{N_{\mathrm{O}}} (|c_{\mathrm{d}} F_{\mathrm{ox}} \Delta U_{\mathrm{ox}}| + |c_{\mathrm{d}} F_{\mathrm{oy}} \Delta U_{\mathrm{oy}}| + |c_{\mathrm{d}} F_{\mathrm{oz}} \Delta U_{\mathrm{oz}}|) \tag{19}$$

where N_{o} denotes the number of nodes, F_{ox}, F_{oy}, and F_{oz} denote the resultant force components of node, ΔU_{ox}, ΔU_{oy}, and ΔU_{oz} denote the incremental displacement components.

2.3. Verification

Based on the CDEM, scholars have carried out extensive research in the fields of impact and blasting and verified the correctness of the method (Wang *et al.*, 2019, Zhang *et al.*, 2020a). In addition, Feng *et al.* (2017), Ju *et al.* (2016), and Zhang *et al.* (2019) verified the correctness of the CDEM in simulation the fracture process by comparing the numerical and experimental results. Therefore, this section mainly details the verification of the correctness of the energy statistics algorithm.

Because of the algorithmic characteristics of the CDEM and the limitations of current laboratory experiments, few types of energy (e.g. element kinetic energy W_{EV}, friction energy W_{R}, and damping energy W_{D}) could not be easily measured in a laboratory. Because the variation trends of some constituent energies during the uniaxial compression process were already analysed by other researchers, this study also chose to perform the uniaxial compression experiment on a sandstone sample for the numerical simulation. The correctness of the algorithm was analysed according to the trends of various constituent energies and the correlation between the cumulative energy value W_{T} and the external work W_{O}. According to theoretical analysis, W_{T} should be equal to W_{O}.

The numerical model was a cylinder (10 cm × 10 cm × 20 cm) of 15,555 elements. The upper and lower surfaces were subjected to velocity boundary conditions ($v = 2\times10^{-9}$ m/s). A linear elastic constitutive model was adopted for the

Table 1. Mechanical parameters of sandstone.

Material	Density (kg/m^3)	Elastic modulus (GPa)	Cohesion strength (MPa)	Tensile strength (MPa)	Friction angle (°)
sandstone	2300	5	5	5	35

elements and a brittle fracture constitutive model for the interfaces. The mechanical parameters shown in Table 1 are the generalised values of sandstone, a few of which (i.e. cohesion strength and friction angle) were derived from *structural geology*, while the rest are empirical values.

The curves of energy variation with respect to fixed mechanical parameters are plotted in Figure 2. Figure 2(a) illustrates the curves of various constituent energies, and Figure 2(b) illustrates the variation curves of W_T and W_O. As observed in the figure, during the initial loading period, the stress increases linearly, and W_{EE} and W_{PE} increase continuously. In addition, W_{EE} is the main component of the model's energy. With the appearance of cracks, the stress and W_{EE} decrease rapidly, while W_R and W_{PC} increase rapidly. At the end of loading ($\varepsilon = 3‰$), the cumulative energy value W_T is 25.96 J, the external work W_O is 25.80 J, and the error value γ is 0.62%.

These trends of various constituent energies and the agreement between W_O and W_T verify the correctness of the energy statistical algorithm.

Since the mechanical parameters of the sandstone sample are not fixed, it is assumed that the cohesion strength and friction angle of sandstone follow the Weibull distribution. Another numerical simulation of the uniaxial compression process was carried out to further verify the correctness of the algorithm.

The curves of energy variation with respect to mechanical properties that satisfy the Weibull criterion are plotted in Figure 3. Figure 3(a) illustrates the trends of various constituent energies, and Figure 3(b) illustrates the trends of W_T and W_O. As in Figure 3(a), the laws of variation of various constituent energies are the same as those in Figure 2(a). At the end of loading ($\varepsilon = 1.5‰$), the cumulative energy value W_T is 5.95 J, the external work W_O is 6.03 J, and the error value γ is 1.28%. Thus, the correctness of the energy statistics algorithm is verified again.

Based on the numerical simulation, it can be concluded that the energy statistics algorithm produces correct results and changes in the mechanical parameters do not affect the correctness of the algorithm.

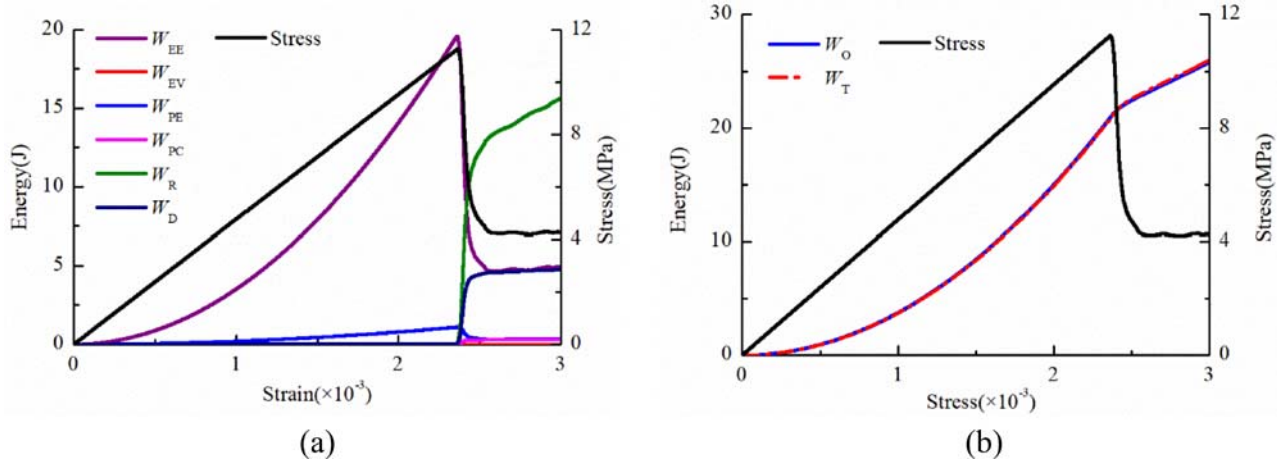

Figure 2. Variation curves of energy and stress of sandstone sample with fixed mechanical parameters.

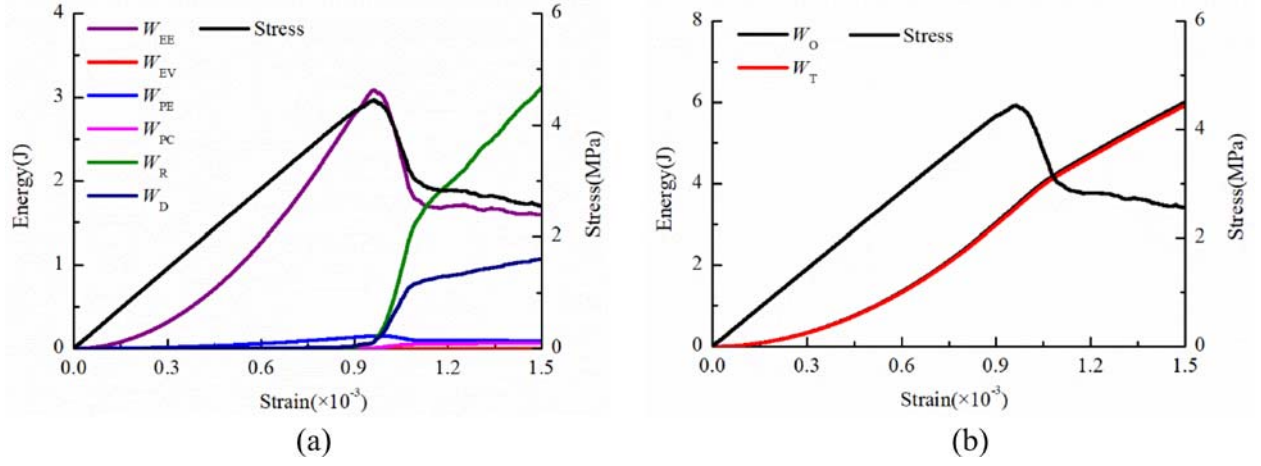

Figure 3. Changing curves of energy and stress of sandstone sample with mechanical parameters satisfying the Weibull distribution.

3. Numerical model and validation

3.1. Numerical model

According to China's 'Technical Standard for Highway Engineering' (JTG B01-2014), highways are divided into five grades: expressway, first-grade highway, second-grade highway, third-grade highway, and fourth-grade highway. The low-grade highway includes third- and fourth-grade highways, and it is generally located near villages and towns.

3.1.1. Modelling

The low-grade highway includes pavement and subgrade, and the pavement is simplified to two or three courses. In this study, because the pavement and impact load areas are symmetrical about the transverse (X direction) and longitudinal directions (Y direction), a quarter three-dimensional numerical model of a low-grade asphalt concrete highway was established (Figure 4). The width of the surface course is 2 m, the widths of the base course and subbase course are 2.5 m, and the dimensions of the subgrade are 8.5 m × 10 m × 9 m. The red area (a quarter circle) at the top of the surface course indicates the impact load area.

3.1.2. Impact load

With the widespread use of vehicle-mounted launching systems, research on launch sites has become more important (Zhao and Jiang, 2018). During missile launch, the launch barrel applies an impact load on the pavement. This study investigates the dynamic responses of a low-grade asphalt concrete highway under impact load caused by the launch barrel. Derived from Feng, Guo, and Yu (2016), the time-history curve of impact load is plotted in Figure 5. The impact load lasts for 1.65 s, with a peak value of 0.79 MPa. The time-history curve has a four-stage characteristic. Stage I lasts from 0 to 0.16 s, during which the impact load increases sharply. Stage II lasts from 0.16 to 0.70 s, during which the impact load remains dynamically stable. Stage III lasts from 0.70 to 1.15 s, during which the impact decreases rapidly. Stage IV lasts from 1.15 to 1.65 s, during which the impact load remains dynamically stable. The load area is a quarter circle with a radius of 1.0 m.

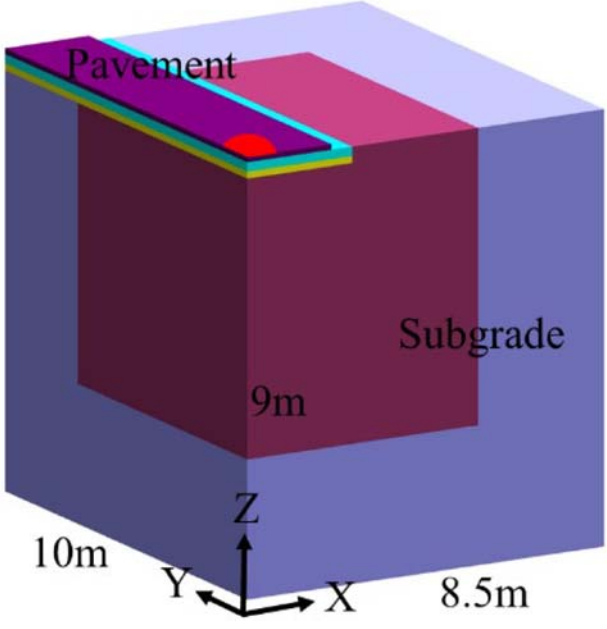

Figure 4. Three-dimensional numerical model of low-grade asphalt concrete highway.

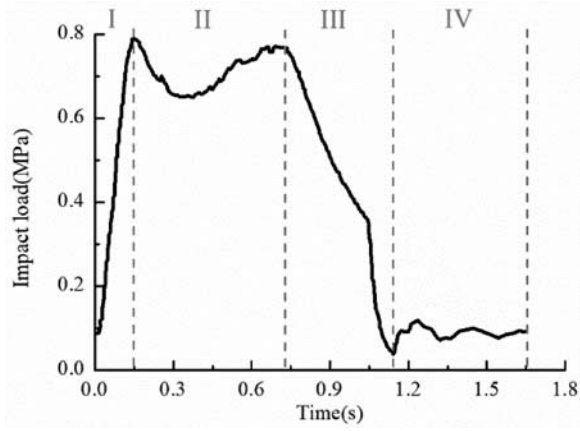

Figure 5. Time-history curve of impact load that applied to pavement.

3.1.3. Simulation scheme

The boundaries are constrained by normal displacement, and a high-damping region with a thickness of 3 m inside the subgrade was set to eliminate the reflection of stress waves.

The numerical calculation included two stages, static calculation stage and dynamic calculation stage. The static calculation stage was used to obtain the initial stress field. To simplify the simulation, this stage only involved analysing the standard design conditions but not the influence of environmental factors. After the static calculation, the displacement was set to zero, which was regarded as the initial case where the low-grade highway was affected only by gravity. Subsequently, the dynamic calculation stage was performed to study the dynamic response.

3.1.4. Mechanical parameters

Because the CDEM includes two basic models (i.e. block and interface), the mechanical parameters include block mechanical parameters as well as interface mechanical parameters. The interface between different courses is a real interface, while the interface inside the course is a virtual interface. The mechanical parameters of the low-grade highway are shown in Table 2. The interface mechanical parameters

Table 2. Mechanical parameters of pavement materials and subgrade.

Material	Density (kg/m^3)	Elastic modulus (GPa)	Cohesive strength (MPa)	Tensile strength (MPa)	Friction angle (°)
Asphalt concrete	2400	0.7	3	0.6	40
Cement stabilised macadam	2410	1.4	1.6	0.4	45
Lime-fly ash stabilised macadam	2200	1.2	1.3	0.35	40
Lime soil	1800	0.4	0.4	0.2	29
Subgrade	1700	0.07	0.04	0.01	20

include the strength class (e.g. cohesion, tensile strength, and friction angle) and stiffness class (e.g. normal stiffness and tangential stiffness). The mechanical parameters of the strength class were obtained according to the weak value of the blocks on both sides. The mechanical parameters of the stiffness class of the virtual interface and the real interface were calculated differently. For the virtual interface, the stiffness is equal to the element stiffness multiplied by 10. For a real interface, the stiffness is equal to $E/\Delta L$, and ΔL denotes the surface roughness.

3.2. Validation

To validate the effectiveness of the CDEM in simulating the deflection of a highway under an impact load, ABAQUS and CDEM were used to simulate the mechanical response of the asphalt concrete highway under impact load.

3.2.1. Basic information

The thickness and material type of each course are listed in Table 3. The contact characteristics of the pavement were simplified, and only the contact between the surface course and base course was considered. In addition, the plastic behaviour was considered in the numerical simulation.

The size, constitutive model, mechanical parameters, and contact characteristics of the numerical model in the CDEM and ABAQUS were the same. By comparing the numerical results of the two methods under the same impact load, the effectiveness of the CDEM in simulating the deflection of a highway under an impact load was validated. The numerical model in the CDEM included 170,500 elements, while the ABAQUS model included 105,050 elements. The time-history curve of the impact load is plotted in Figure 6. The load lasted for 2.0 s, with peak value at 0.17 MPa.

Table 3. Thickness and material type of each course in the pavement structure.

Type	Thickness/(cm)	Material
Surface course	10	Asphalt concrete
Base course	20	Cement stabilised macadam
Subbase course	15	Lime soil

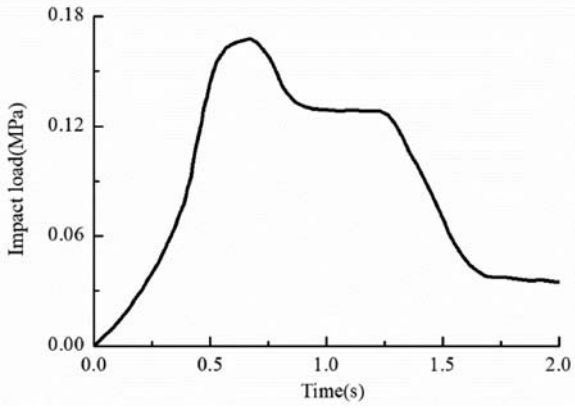

Figure 6. Time-history curve of impact load.

3.2.2. Data analysis

The time-history curve of deflection at the load centre is plotted in Figure 7, and the deflection values of the load centre point at different moments are shown in Table 4.

According to Figure 7 and Table 4, the deflection as calculated by the CDEM is consistent with that calculated by ABAQUS. This consistency is reflected in the same deflection trend and similar deflection values at several typical moments in CDEM and ABAQUS, and the maximum error of deflection is 2.94%.

Thus, based on the comparison of numerical results, the effectiveness of CDEM in simulating the deflection of a highway under an impact load was validated.

ABAQUS is considered a powerful finite element software. However, because of the limitations of its numerical algorithm, the software cannot be used to simulate the process of crack generation and propagation inside the surface course, base course, and subbase course. However, the CDEM's numerical algorithm does not have this disadvantage. Therefore, CDEM is selected for the numerical simulation.

4. Results and discussion

An asphalt concrete highway as recommended in the *Instruction Manual of Rural Road Construction in Henan Province* was selected for the numerical simulation. The thickness and material type of each course are shown in Table 5, and the pavement structure is shown in Figure 8. To realistically

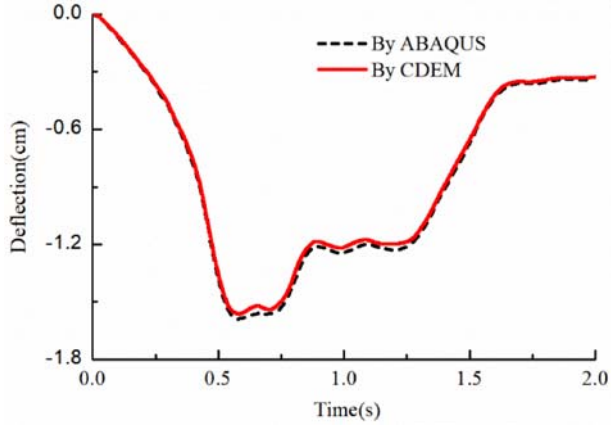

Figure 7. Time-history curves of deflection as calculated by ABAQUS and CDEM.

Table 4. Deflection values of load centre point at different moments.

	Deflection/(cm)	
Time	By CDEM	By ABAQUS
0.58s	−1.56	−1.59
1.23s	−1.19	−1.22
1.68s	−0.35	−0.36
2.0s	−0.33	−0.34

Table 5. Thickness and material type of each course in the pavement structure.

Pavement structure	Surface course	Base course	Subbase course
Asphalt concrete	10 cm asphalt concrete	10 cm lime-fly ash stabilised macadam	15 cm lime soil

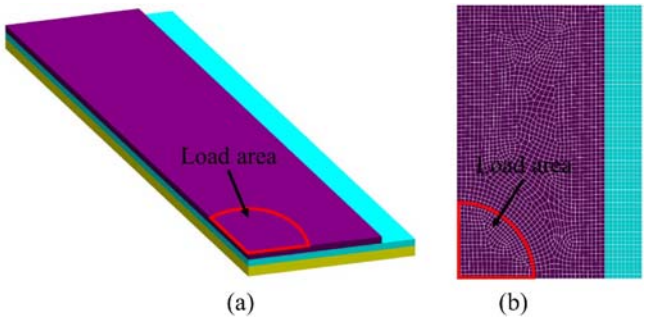

Figure 8. Three-dimensional numerical model of asphalt concrete pavement structure.

simulate the process of crack generation and propagation, the interfaces between different courses, between different elements inside each course, and between pavement and subgrade were considered.

4.1. Evolution characteristic of deflection and deformation

4.1.1. Evolution characteristic of deflection

The deflection nephograms at different moments are shown in Figure 9, which clearly depicts the transition of deflection from continuous distribution to discontinuous distribution. Since the impact load area is a quarter circle, the deflection at the top of the surface course is distributed circularly, and the maximum deflection is located at the load centre. With the appearance of cracks, the deflection nephograms begin to exhibit discontinuous features because the stress transmission is affected.

To analyse the distribution characteristics of deflection at the top of the surface course in more detailed, the deflection curves along the X and Y directions are plotted in Figure 10. Because the deflection at the top of the surface course is distributed circularly, the deflection curves along the X and Y directions are the same. At $t = 0.16$ s and $t = 1.65$ s, the deflection curves along the X and Y directions have an inflection point, which indicates the discontinuous distribution characteristics of deflection. As indicated in Figure 9, the inflection point is located outside the ring-shaped crack plane. Although the impact load area and boundary conditions are symmetrical, the deflection curves in the X and Y directions have minute differences because the geometric dimensions of the surface course along the two directions are not the same.

Based on the above analysis, the maximum deflection is located on the load centre. To analyse the trend of deflection and the correlation between deflection and impact load, the time-history curve of deflection on the load centre is plotted in Figure 11. The time-history curve of deflection has a four-stage characteristic, and its variation trend is closely related to the impact load. The maximum instantaneous deflection is located at the junction of Stages I and II, which corresponds to the peak value of impact load.

The time-history curves of deflection at different depths are plotted in Figure 12. The coordinate value on the top of the surface course is Z = 0.35 m, the coordinate value at the interface between subgrade and the subbase course is Z = 0 m, and the coordinate value at the bottom of subgrade is Z = −9 m. As observed from the figure, deflection occurs at different depths with different values. Meanwhile, the deflection gradually decreases from the top of the surface course to the bottom of subgrade. The time-history curves of deflection of pavement and the upper part of subgrade also possess a four-stage characteristic, and their variation trend is closely related to the impact load. The deflection value on the top of the surface course and the top of subgrade is nearly the same, which suggests that the pavement structure underwent a small deformation. For subgrade, different depths have different

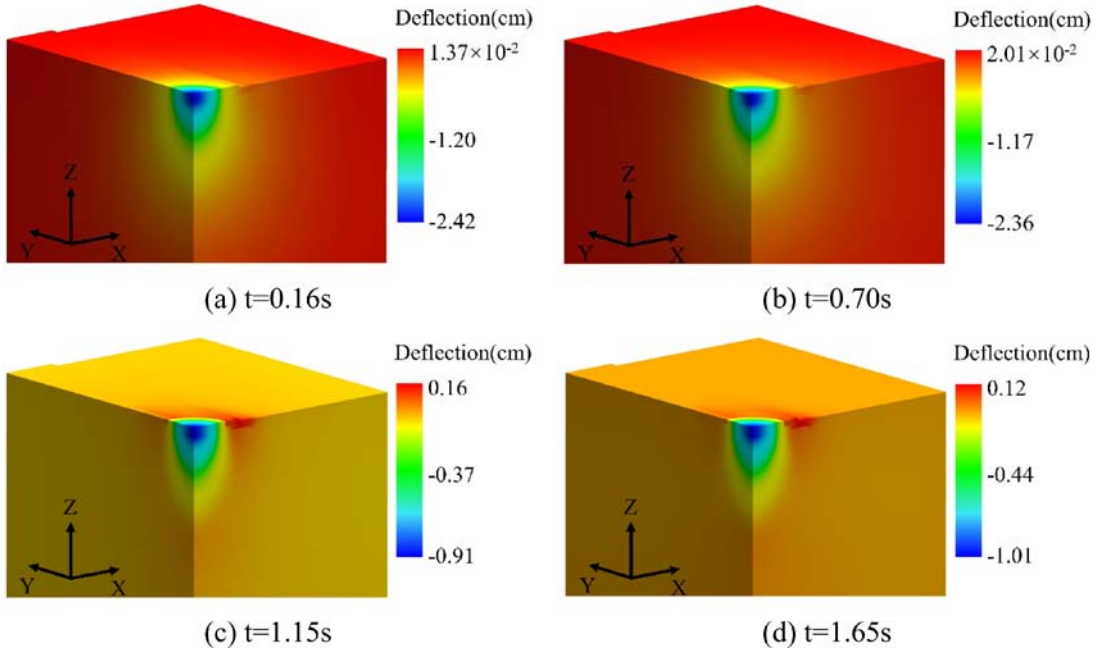

Figure 9. Deflection nephograms of asphalt concrete highway at different moments.

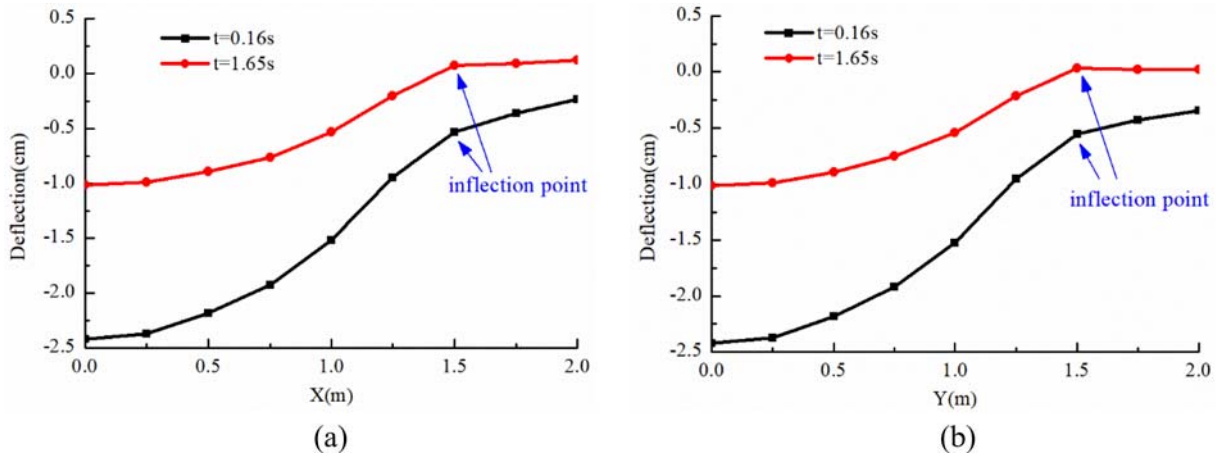

Figure 10. Deflection curves along the X and Y directions at the top of surface course.

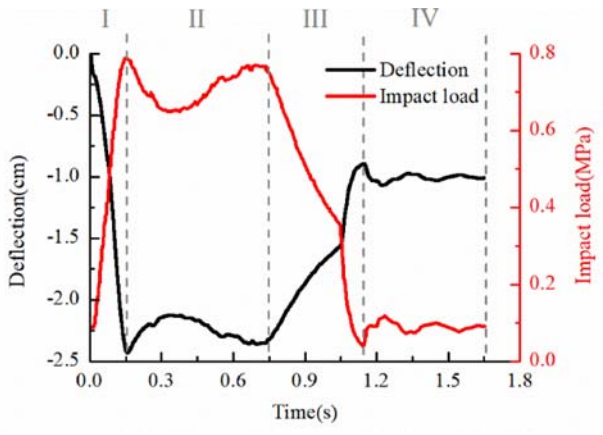

Figure 11. Time-history curve of deflection at the impact load centre.

deflections. When the difference in depth is the same, the difference in deflection is large at the upper part of subgrade and small at the bottom.

4.1.2. Evolution characteristic of deformation

Because the deflection at the top of the surface course is caused by the compressive deformation of pavement and subgrade, the deformation value of each depth range from the top of the surface course to the bottom of subgrade were analysed. According to the analysis, deflections at the top of the surface course and the bottom of the subbase course were nearly the same. Therefore, the pavement was considered as a whole, and the subgrade was divided into six depth ranges. The depth was represented by the coordinate value in the Z direction.

The time-history curves of deformation in different depth ranges are plotted in Figure 13, and the negative value denotes the compressive deformation. Because the deformation value is small, it is reported in centimetre. Figure 13 illustrates that the pavement and subgrade are deformed under impact load, but the deformation in different depth ranges is significantly different. The time-history curves of deformation have a four-stage characteristic, and the changing trend is closely related to the impact load. In addition, with the increase in depth, the stage characteristics gradually weaken. At the same time, the deformation value gradually decreases from top to bottom, which indicates that the influence of the impact load weakens.

Figure 14 illustrates the ratio of deformation in different depth ranges to the total deformation of highway at different moments. As shown in Figure 14, the total deformation of highway is mainly caused by the upper part of subgrade. The deformation in the range of −1.5 to 0 m accounts for 60% of the total deformation, and the deformation in the range of −3 to −1.5 m accounts for 30% of the total deformation. It

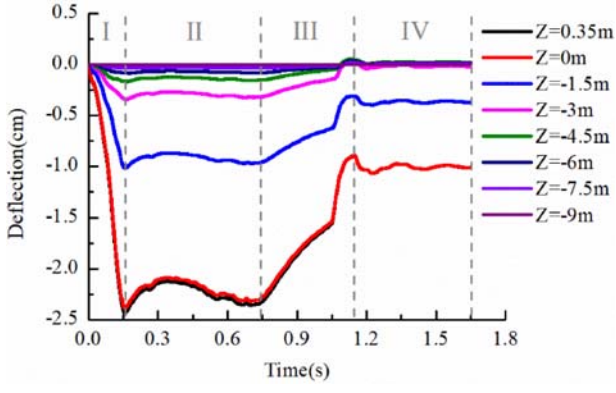

Figure 12. Time-history curves of deflection at different depths.

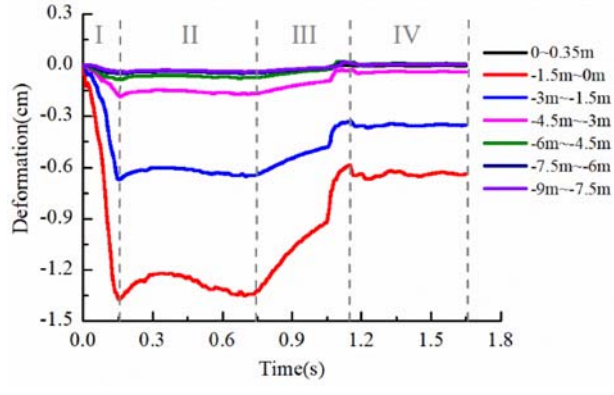

Figure 13. Time-history curves of deformation in different depth ranges.

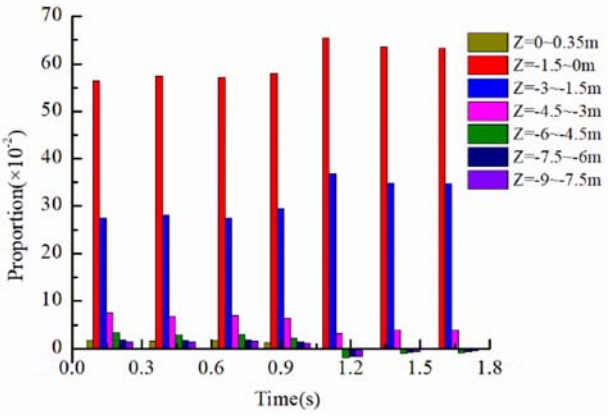

Figure 14. Deformation proportion in different depth ranges at different moments.

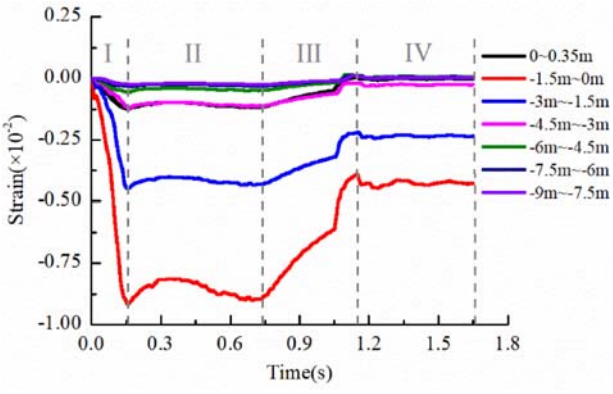

Figure 15. Time-history curves of compressive strain in different depth ranges.

can be seen that the proportion of these two ranges is close to 90%, and there are slight fluctuations.

The time-history curves of strain in different depth ranges are plotted in Figure 15, and the negative value represents compressive strain. It can be observed that strain occurs in pavement and different depth ranges of subgrade, but the value is significantly different. The time-history curves have a four-stage characteristic, and the changing trend is closely related to impact load. In addition, with the increase in depth, the stage characteristics gradually weaken. Although the mechanical parameters of pavement are better than those of subgrade, the absolute value of its strain is not the smallest, and this is because pavement directly bears impact load. The pavement transmits and diffuses impact load, and the upper part of subgrade absorbs considerable amount of impact energy. Therefore, the strain value at the bottom of subgrade is the smallest.

4.2. Evolution characteristic of crack

4.2.1. Crack ratio α_D

The crack ratio α_D is a dimensionless index that represents the failure state, and its time-history curve is plotted in Figure 16. The crack planes in the pavement structure at t=0.16 s and t=1.65 s are shown in Figure 17 (black line indicates the

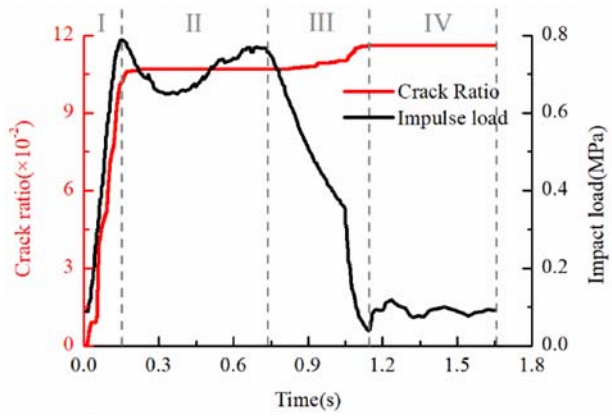

Figure 16. Time-history curve of crack ratio α_D.

crack plane). Since the impact load area is a quarter circle, there is a ring-shaped crack plane in the surface course. The time-history curve of crack ratio α_D has a four-stage characteristic, and the change in α_D is closely related to that of the impact load. The crack ratio α_D=10.40% at t=0.16 s and α_D=11.62% at t=1.65 s, which means that the new crack planes appearing from 0 s to 0.16 s account for 89.50% of the overall crack planes. Therefore, it can be concluded that, although the sharp increase and decrease in the impact load will lead to an increase in the crack ratio α_D, the crack planes mainly appear when the impact load increases rapidly.

4.2.2. Spatial distribution and failure type

The initial failure type nephograms of the surface course, base course and subbase course are plotted in Figure 18–20.

Figure 18 illustrates the initial failure type and distribution characteristic of the crack planes of the surface course. It can be observed that the crack planes include a ring-shaped crack plane and crack planes along the X and Y directions, and the ring-shaped crack plane inside the surface course is located outside the impact load area. In addition, the crack planes mainly occur when the impact load increases rapidly (0 s–0.16 s), and all the crack planes appearing from 0 s to 0.16 s are vertical. There are still new crack planes appearing from 0.16 s to 1.65 s, but the number is small. Moreover, the new crack planes appearing in this period include not only some vertical crack planes but also some horizontal crack planes between the surface course and base course. The initial failure type of all crack planes is tensile failure.

Figure 19 illustrates the initial failure type and distribution characteristic of the crack planes of the base course. It can be observed that the crack planes mainly occur when the impact load increases rapidly (0 s–0.16 s), and these crack planes appear inside the base course, between the base course and subbase course, and between the base course and subgrade. In addition, the crack planes inside the base course mainly include a ring-shaped crack plane, radial crack planes, and crack planes along the X and Y directions. The ring-shaped crack planes inside the surface course and base course have the same position in the horizontal level. The initial failure types of crack planes include tensile failure and shear failure. The crack planes inside the base course, between the base

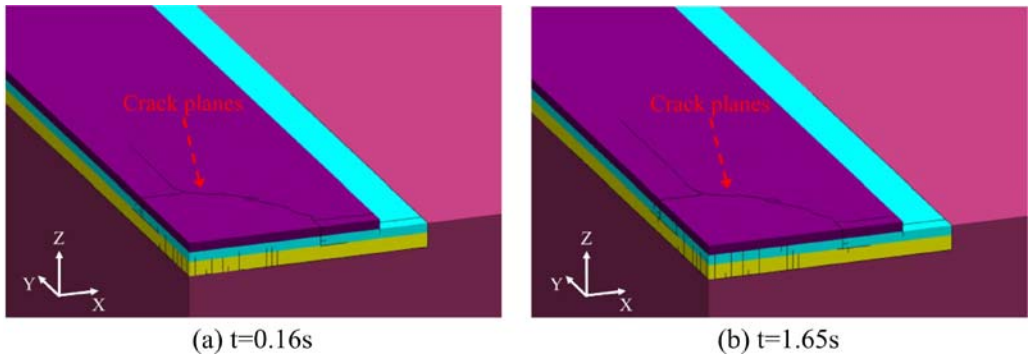

Figure 17. Spatial distribution of crack planes at different moments (black line indicates crack plane).

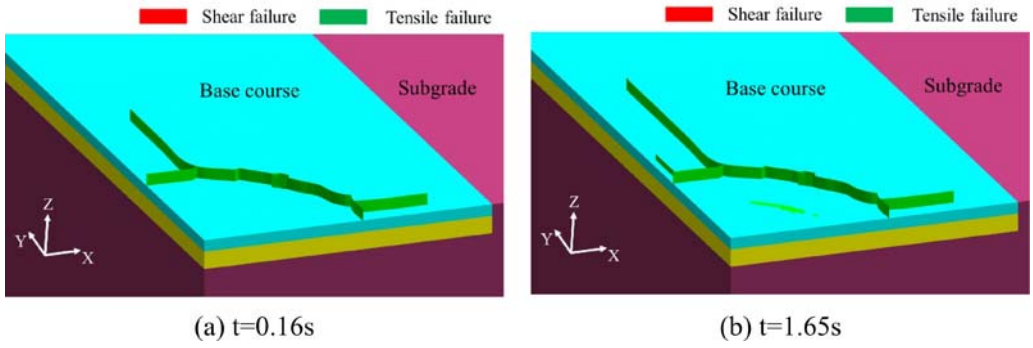

Figure 18. Initial failure type nephogram of cracks in surface course at different moments.

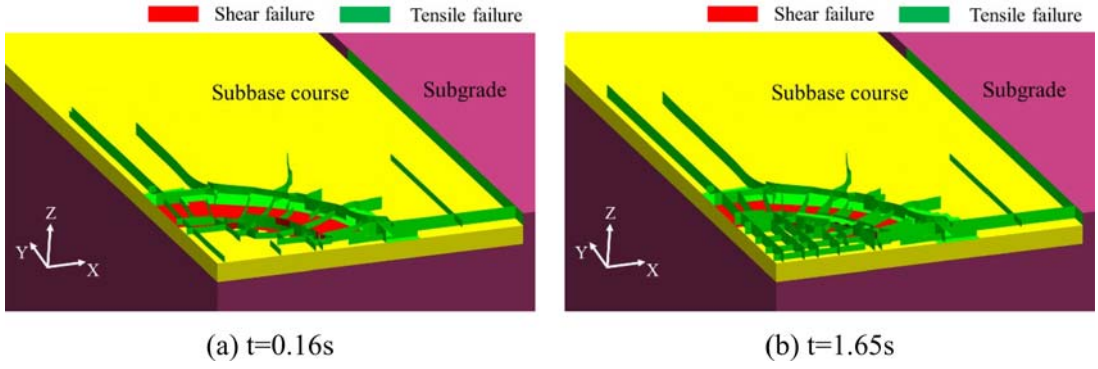

Figure 19. Initial failure type nephogram of cracks in base course at different moments.

course and surface course, and between the base course and subgrade are tensile failures. The crack planes between the base course and subbase course are divided by the ring-shaped crack plane. The crack planes inside the ring-shaped crack plane are mainly shear failure, while the crack planes outside the ring-shaped crack plane are mainly tensile failures.

Figure 20 illustrates the initial failure type and distribution characteristic of the crack planes of the subbase course. As observed in the figure, the crack planes mainly occur when the impact load increases rapidly (0–0.16 s), and these crack planes appear inside the subbase course, between the subbase course and base course, and between the subbase course and subgrade. In addition, the crack planes inside the subbase course mainly include a ring-shaped crack plane, radial crack planes, and crack planes along the X and Y directions. The ring-shaped crack planes inside the surface course, base course, and subbase course have the same position in the horizontal level, and they are located outside the impact load area. The initial failure types of crack planes include tensile failure and shear failure. The type of failure of crack planes inside the subbase course is mainly tensile failure, and only a few crack planes undergo shear failure. The ring-shaped crack plane inside the subbase course undergoes shear failure. The crack planes between the subbase course and subgrade mainly undergo shear failure, while only a few crack planes undergo tensile failures.

According to Figures 18–20, the subbase course undergoes more severe damage than the surface course. According to Table 2, a few mechanical parameters (e.g. cohesion strength, tensile strength, and friction angle) of the surface course are

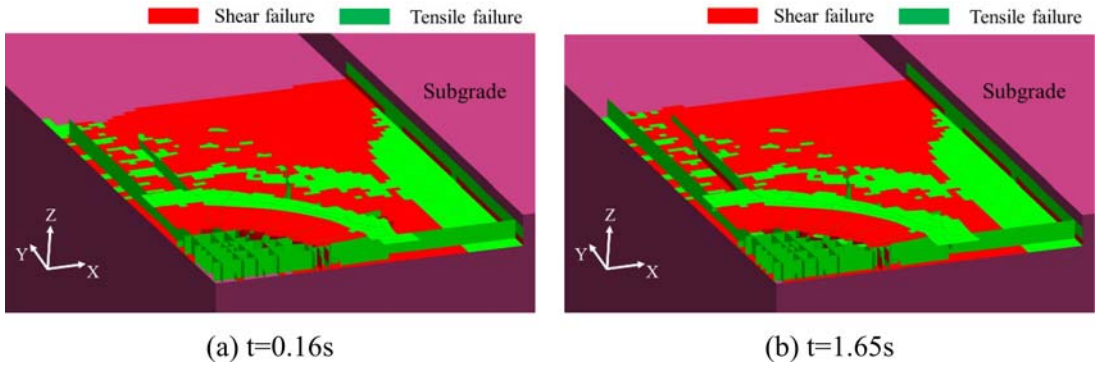

Figure 20. Initial failure type nephogram of cracks in subbase course at different moments.

significantly stronger than those of the subbase course. These parameters are the key factors affecting the cracks at the interfaces. The numerical results reveal that the stress state of the surface course is similar to that of the subbase course. Therefore, the subbase course suffers more severe damage than the surface course.

4.3. Evolution characteristic of energy

4.3.1. Cumulative energy value W_T

The time-history curve of the cumulative energy value W_T is plotted in Figure 21. Due to the influence of gravity, W_T is not zero at the initial moment when the impact load is applied to the pavement. As illustrated in Figure 21, the time-history curve of W_T has a four-stage characteristic, and its variation trend is consistent with that of the impact load. The maximum W_T is located at the junction of Stages I and II, which corresponds to the peak value of the impact load.

4.3.2. Various constituent energies

The time-history curve of element deformation energy W_{EE} is plotted in Figure 22(a). It has a four-stage characteristic, and its variation trend is consistent with that of the impact load. The maximum W_{EE} is located at the junction of Stages I and II, which corresponds to the peak value of the impact load. The law of variation of W_{EE} was analysed briefly. As shown in Figure 15, the strain of the pavement and subgrade increases sharply with the sharp increase in impact load, and consequently, W_{EE} increases. Then, the impact load remains dynamically stable, and the strain of pavement and subgrade is also dynamically stable. Therefore, W_{EE} does not change significantly. Subsequently, with the sharp decrease in impact load, the strain of the pavement and subgrade decreases rapidly. Thus, W_{EE} decreases sharply. Finally, the impact load remains dynamically stable. Thus, the strain and W_{EE} also remain dynamically stable.

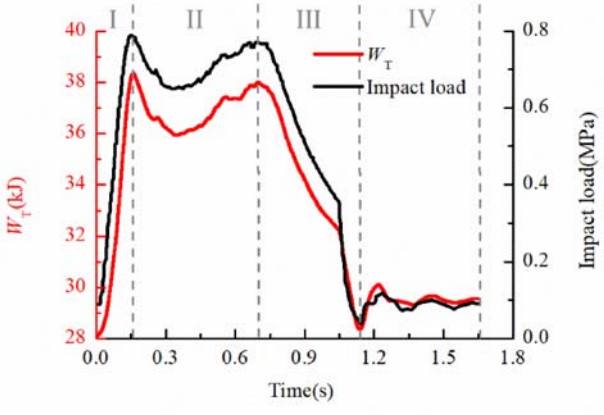

Figure 21. Time-history curve of cumulative energy value W_T of entire highway.

The time-history curve of the element kinetic energy W_{EV} is plotted in Figure 22(b). The time-history curve has two peaks that occur in the period of sharp increase and decrease in impact load, respectively. When the impact load is dynamically stable, W_{EV} is nearly 0. In addition, the maximum W_{EV} is in the period of a sharp increase in the impact load. The law of variation of W_{EV} is briefly analysed. According to Figure 23, W_{EV} is mainly generated near the impact load area. Figure 24 illustrates the time-history curve of velocity at the centre of the impact load area. During the period of rapid increase in impact load, the deflection increases sharply, while the velocity first increases sharply and then decreases, resulting in the occurrence of the first peak of W_{EV}. During the period of dynamic stability of the impact load, deflection remains dynamically stable and velocity is nearly 0, and thus W_{EV} is nearly 0. In the initial moments of the period of a sharp decrease in the impact load, deflection decreases slowly, and thus velocity is still 0. However, when deflection decreases rapidly, the velocity increases abruptly, resulting in the second peak of W_{EV}. Finally, when deflection is dynamically stable, the velocity is 0, and thus W_{EV} is nearly 0.

The time-history curve of the spring deformation energy W_{PE} is plotted in Figure 22(c). It can be observed that the curve has a four-stage characteristic, and the variation trend is consistent with that of the impact load. The maximum W_{PE} is located at the junction of Stages I and II, which corresponds to the peak value of the impact load. A brief analysis of the changing law of W_{PE} was conducted. The interaction of elements on both sides of the interface is transferred by the numerical springs. When the impact load increases sharply, the displacement and deformation of elements increase, which enhances the interaction between elements. Thus, W_{PE} increases. Then, the impact load, as well as the interaction between elements, remains dynamically stable. Therefore, W_{PE}

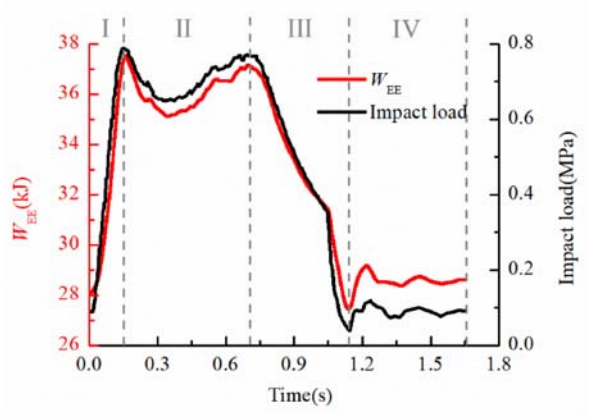

(a) the time-history curve of element deformation energy W_{EE}

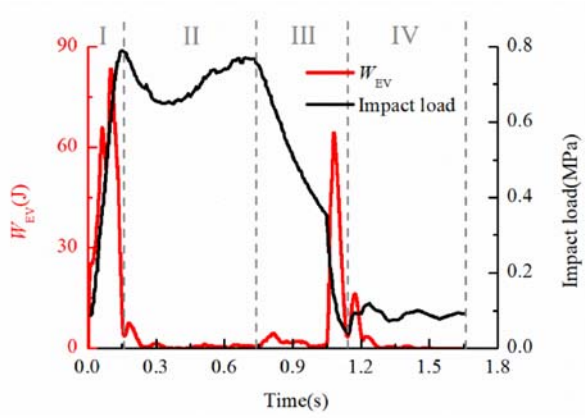

(b) the time-history curve of element kinetic energy W_{EV}

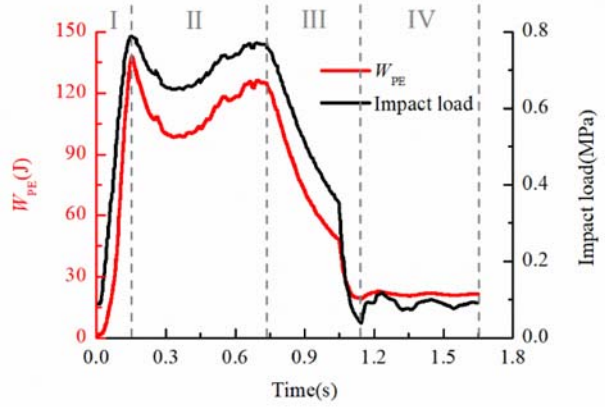

(c) the time-history curve of spring deformation energy W_{PE}

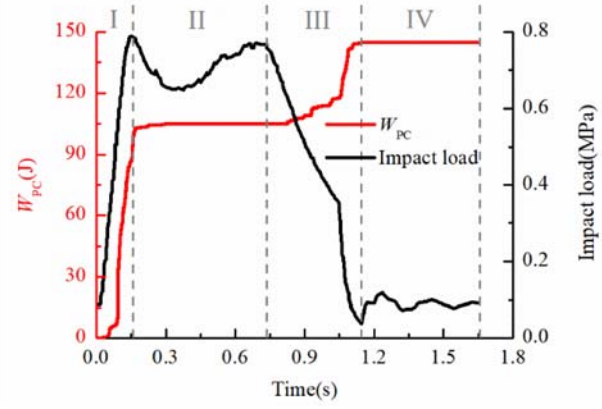

(d) the time-history curve of spring fracture energy W_{PC}

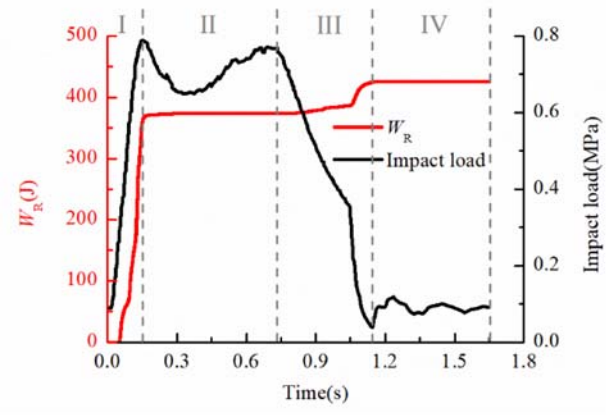

(e) the time-history curve of friction energy W_R

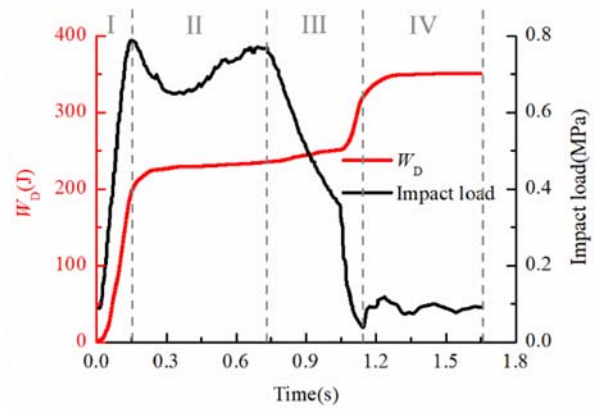

(f) the time-history curve of damping energy W_D

Figure 22. Time-history curves of various constituent energies of entire highway.

does not change significantly. Subsequently, the impact load decreases sharply, starkly weakening the interaction between elements. Therefore, W_{PE} decreases. Finally, the impact load remains dynamically stable, and the interaction between elements no longer changes significantly. Hence, W_{PE} remains dynamically stable.

The time-history curve of the spring fracture energy W_{PC} is plotted in Figure 22(d). The curve has a four-stage characteristic, and the variation trend is closely related to that of the impact load. The sharp increase and decrease in the impact load lead to an obvious increase in the spring fracture energy W_{PC}, but W_{PC} mainly increases when the impact load

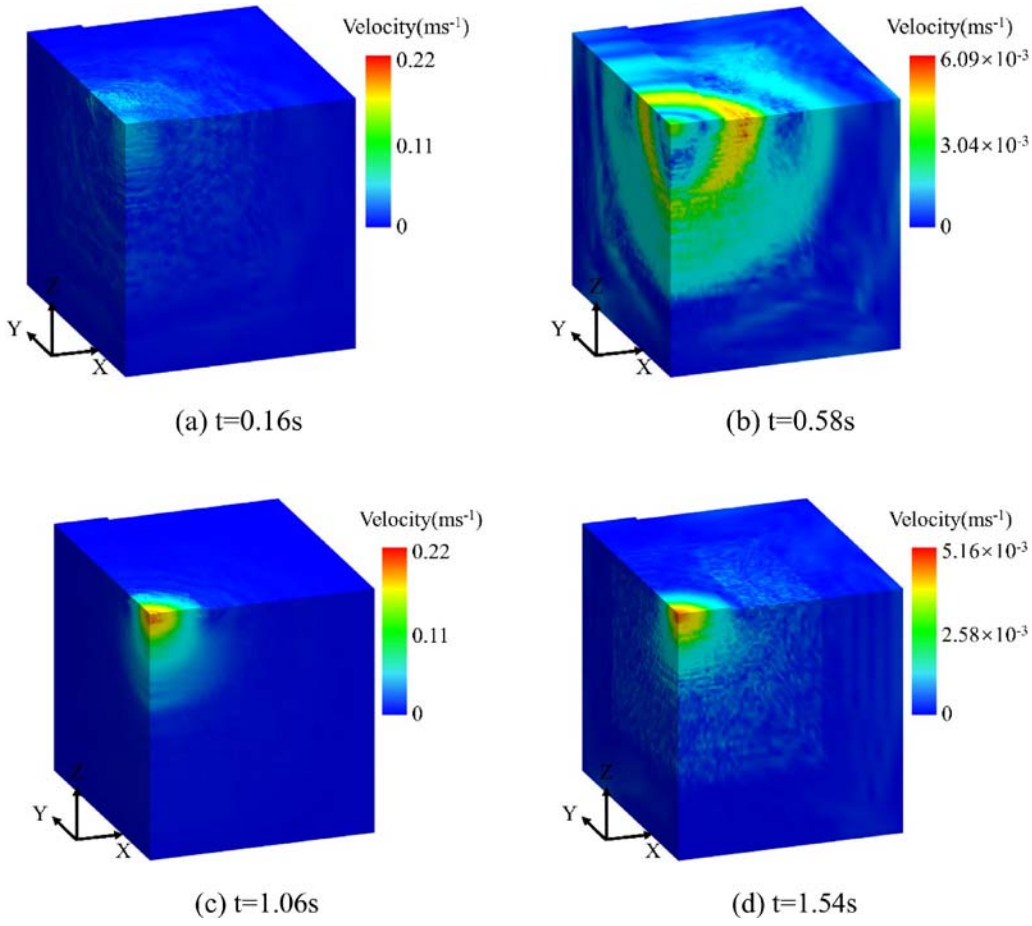

Figure 23. Velocity nephograms of the entire highway at different moments.

increases sharply. A brief analysis of the changing law of W_{PC} was conducted. Based on the results of Equations (13)–(16), it is concluded that W_{PC} is closely related to the crack area S_c. When the mechanical parameters of the interfaces are the same or similar, W_{PC} is approximately linearly related to the crack area S_c. Figure 16 illustrates crack planes appearing when the impact load increases or decreases sharply. In addition, crack planes that appear from 0 to 0.16 s have a larger area than the crack planes that appear from 0.70 to 1.15 s. Therefore, the time-history curve of W_{PC} has the four-stage characteristic.

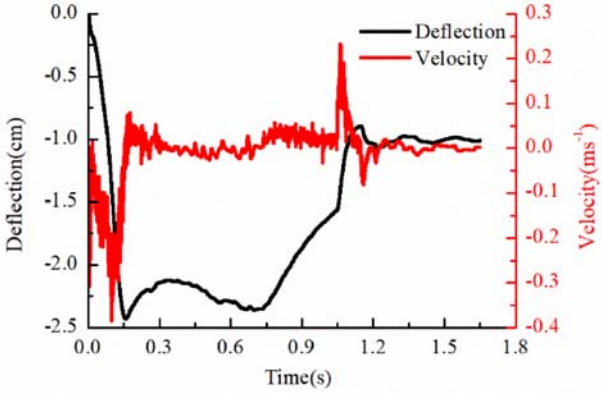

Figure 24. Time-history curve of velocity at the impact load centre.

Figure 22(e) illustrates the time-history curve of the friction energy W_R. The curve also has a four-stage characteristic, and the variation trend is closely related to that of the impact load. The sharp increase and decrease in the impact load lead to an increase in W_R. However, W_R mainly increases when the impact load increases sharply. The law of variation of W_R was briefly analysed. Based on the results of Equation (17), it is concluded that W_R is only generated at the crack planes, and its value is closely related to the relative tangential displacement. As the impact load increases sharply, the area of the crack planes and the relative tangential displacement also increase sharply. Therefore, W_R increases strongly. The impact load remains dynamically stable, although the area of the crack planes is large. The relative tangential displacement remains small. Therefore, W_R remains unchanged. Subsequently, the impact load plummets, and the area of the crack planes and the relative tangential displacement surge. Therefore, W_R witnesses a strong surge again. Finally, the impact load remains dynamically stable, and the W_R does not increase significantly.

The time-history curve of the damping energy W_D is plotted in Figure 22(f). The curve has a four-stage characteristic, and the variation trend is closely related to that of the impact load. In addition, W_D mainly increases when the impact load increases sharply. The law of variation of W_D was briefly analysed. Based on the results of Equation (18), it is observed that W_D is closely related to the nodal resultant force and incremental displacement. When the impact load

increases sharply, the nodal resultant force and incremental displacement increase accordingly. Therefore, W_D increases sharply. Then, the impact load remains dynamically stable. Although the nodal resultant force is large, the incremental displacement remains small. Hence, W_D increases slowly. Subsequently, the impact load decreases sharply. Although the nodal resultant force decreases, as a result, the incremental displacement increases sharply, and therefore, W_D resurges. Finally, the impact load becomes dynamically stable, and W_D does not change significantly.

This analysis shows that, although the trends of various constituent energies are different, they are all closely related to the change in impact load.

Although some of the above results have been revealed in the previous studies, this study in this article is more in-depth. The evolution characteristics of crack and energy are innovative content. Based on the evolution characteristics of deflection and strain, it can be concluded that improving the stiffness of subgrade (especially the upper part of subgrade) is a more effective means to reduce the deflection of pavement under impact load. Based on the evolution characteristics of crack, it can be seen that strengthening the shear strength of pavement materials is an effective means to prevent serious road damage. In addition, it can help engineers understand how to optimise the equipment to enhance the pavement crushing effect during the rehabilitation, demolition, and reconstruction process. Based on the evolution characteristics of energy, it is not only possible to evaluate the energy utilisation rate (i.e. the ratio of fracture energy to total energy) in the pavement crushing process and improve the crushing effect of the equipment, but also to lay the foundation for a more in-depth study of the energy conversion mechanism.

5. Conclusions

Based on the CDEM, this study investigated the evolution characteristics of deflection, crack, and energy of a low-grade asphalt concrete highway under impact load. First, an energy statistics algorithm was proposed, and its correctness was verified. Then, a quarter three-dimensional numerical model of a low-grade asphalt concrete highway was established. Finally, numerical simulation of the low-grade asphalt concrete highway under impact load was conducted, and the evolution characteristics were analysed in detail. The following conclusions were drawn from the results of the analysis:

(1) The trends of deflection and deformation are consistent with those of the impact load, and the maximum instantaneous deflection corresponds to the peak value of the impact load. In addition, as the depth increases, deflection and deformation gradually decrease. The deformation in the range of −1.5 to ∼0 m and −3 to ∼ −1.5 m accounted for 60% and 30% of the total deformation, respectively.
(2) The crack ratio α_D mainly increases when the impact load increases sharply. The cracks are distributed near the impact load area, and mainly include a ring-shaped crack plane, radial crack planes, and crack planes along the X and Y directions. Moreover, the initial failure types of crack planes include tensile failure and shear failure. Moreover, the type of failure differ between different courses.
(3) The changing trend of the *cumulative energy value* W_T is consistent with that of the impact load, and the maximum of W_T corresponds to the peak value of the impact load. For various constituent energies, the laws of variation of different constituent energies are different, but their changes are all closely related to the change in impact load.

In future research, the correctness of the energy statistics algorithm should be verified by field experiments, and a viscosity term should be introduced into the constitutive model to study the mechanical response of asphalt concrete highways at high temperatures. Meanwhile, the characteristics of deformation within the depth of 0–1 m and the failure mechanism of pavement should be analysed in detail. In addition, a study on the mechanical response of cement concrete highways should be conducted, and field experiments should be performed to verify the correctness of the crack pattern.

Disclosure statement

No potential conflict of interest was reported by the author(s).

Funding

This work was supported by Ministry of Science and Technology of the People's Republic of China [grant number 2018YFC1505504].

Data availability statement

Data in this manuscript is good to offer, if there is any request, please contact the corresponding author.

References

Alisjahbana, S.W., *et al.*, 2018. Dynamic response of pavement plates to the positive and negative phases of the Friedlander load. *Strength of Materials*, 50 (5), 702–710. doi:10.1007/s11223-018-0015-5

Assogba, O.C., *et al.*, 2020. Numerical investigation of the mechanical response of semi-rigid base asphalt pavement under traffic load and nonlinear temperature gradient effect. *Construction and Building Materials*, 235 (2020), 117406. doi:10.1016/j.conbuildmat.2019.117406

Ceylan, H., *et al.*, 2008. Rehabilitation of concrete pavements utilizing rubblization: a mechanistic based approach to HMA overlay thickness design. *International Journal of Pavement Engineering*, 9 (1), 45–57. doi:10.1080/10298430701201260

Ebrahimi-Mamaghani, A., Sarparast, H., and Rezaei, M, 2020. On the vibrations of axially graded Rayleigh beams under a moving load. *Applied Mathematical Modelling*, 84 (2020), 554–570. doi:10.1016/j.apm.2020.04.002

Feng, C., *et al.*, 2014. A semi-spring and semi-edge combined contact model in CDEM and its application to analysis of Jiweishan landslide. *Journal of Rock Mechanics and Geotechnical Engineering*, 6 (1), 26–35. doi:10.1016/j.jrmge.2013.12.001

Feng, C., *et al.*, 2017. Numerical simulation for penetrating and blasting process of EPW based on CDEM. *Journal of Vibration and Shock*, 36 (13), 11–26.

Feng, J., Guo, Z., and Yu, Z., 2016. Discussion on settlement calculation methods of the low level asphalt pavement under action of impact load. *Chinese Journal of Underground Space and Engineering*, 12 (2), 889–893.

Ge, Z., *et al.*, 2015. Properties of cold mix asphalt mixtures with reclaimed granular aggregate from crushed PCC pavement. *Construction and*

Building Materials, 77 (2015), 404–408. doi:10.1016/j.conbuildmat.2014.12.084

Gu, X., *et al*., 2014. Dynamic response of pavement under FWD using spectral element method. *KSCE Journal of Civil Engineering*, 18 (4), 1047–1052. doi:10.1007/s12205-014-0298-4

Holl, A., and Mariotti, I, 2018. Highways and firm performance in the logistics industry. *Journal of Transport Geography*, 72 (2018), 139–150. doi:10.1016/j.jtrangeo.2018.08.021

Huang, T., Ma, D., and Zhang, Z, 2017. Research on modeling and dynamic response of launching site based on ABAQUS. *Journal of Gun Launch and Control*, 38 (1), 22–27.

Iqbal, M.A., Kumar, V., and Mittal, A.K, 2019. Experimental and numerical studies on the drop impact resistance of prestressed concrete plates. *International Journal of Impact Engineering*, 123 (2019), 98–117. doi:10.1016/j.ijimpeng.2018.09.013

Jha, M.K., *et al*., 2012. Maximizing resource effectiveness of highway infrastructure maintenance inspection and scheduling for efficient city logistics operations. *Procedia - Social and Behavioral Sciences*, 39 (2012), 831–844. doi:10.1016/j.sbspro.2012.03.151

Ju, Y., *et al*., 2016. CDEM-based analysis of the 3D initiation and propagation of hydrofracturing cracks in heterogeneous glutenites. *Journal of Natural Gas Science and Engineering*, 35 (2016), 614–623. doi:10.1016/j.jngse.2016.09.011

Liang, R., and Zeng, S, 2002. Efficient dynamic analysis of multilayered system during falling weight deflectometer experiments. *Journal of Transportation Engineering*, 128 (4), 366–374. doi:10.1061/(ASCE)0733-947X(2002)128:4(366)

Liu, N., *et al*., 2018. Influence of interface conditions on the response of transversely isotropic multi-layered medium by impact load. *Journal of the Mechanical Behavior of Biomedical Materials*, 77, 485–493. doi:10.1016/j.jmbbm.2017.09.034

Liu, L., *et al*., 2019. Numerical analysis of rehabilitated concrete pavement using crack-and-seating technique. *International Journal of Pavement Engineering*, 1–13.

Luo, W., Xia, Y., and Weng, S, 2015. Vibration of Timoshenko beam on hysteretically damped elastic foundation subjected to moving load. *Science China Physics, Mechanics & Astronomy*, 58 (8), 1–9.

Picoux, B., El Ayadi, A., and Petit, C, 2009. Dynamic response of a flexible pavement submitted by impulsive loading. *Soil Dynamics and Earthquake Engineering*, 29 (5), 845–854. doi:10.1016/j.soildyn.2008.09.001

Ren, J., *et al*., 2014. Study on elasto-plastic response of the unsupported random launching site for the missile. *Advanced Materials Research*, 945-949 (2014), 1274–1279. doi:10.4028/www.scientific.net/AMR.945-949.1274

Sun, L., and Duan, Y, 2013. Dynamic response of top-down cracked asphalt concrete pavement under a half-sinusoidal impact load. *Acta Mechanica*, 224 (8), 1865–1877. doi:10.1007/s00707-013-0849-7

Szyłko-Bigus, O., Śniady, P., and Zakęś, F., 2019. Application of Volterra integral equations in the dynamics of a multi-span Rayleigh beam subjected to a moving load. *Mechanical Systems and Signal Processing*, 121 (2019), 777–790. doi:10.1016/j.ymssp.2018.11.056

Timoshenko, S.P, 1921. LXVI. *On the correction for shear of the differential equation for transverse vibrations of prismatic bars. The London, Edinburgh, and Dublin Philosophical Magazine and Journal of Science*, 41 (245), 744–746. doi:10.1080/14786442108636264

Timoshenko, S.P, 1922. X. *On the transverse vibrations of bars of uniform cross-section. The London, Edinburgh, and Dublin Philosophical Magazine and Journal of Science*, 43 (253), 125–131. doi:10.1080/14786442208633855

Wang, H., *et al*., 2019. An efficient CDEM-based method to calculate full-scale fragment field of warhead. *International Journal of Impact Engineering*, 133 (2019), 103331. doi:10.1016/j.ijimpeng.2019.103331

Wei, X., *et al*., 2017. The impact of concrete pavement field floor to vehicle missile launching process. *International Journal of Aerospace Engineering*, 2017, 1–11.

Westergaard H.M., 1926. Stresses in concrete pavements computed by theoretical analysis. *Public Roads*, 7 (2), 25–35

Westergaard H.M., 1933. Analytical tools for judging results of structural tests of concrete pavement. *Public Roads*, 14 (10), 185–188.

Westergaard H.M., 1939. Stresses in concrete runways of airports. In: *Proceedings of 19th annual meeting, highway research board*, Washington D C, 197–205.

Westergaard H.M., 1948. New formulas for stresses in concrete pavements of airfields. *ASCE Transactions*, 113, 425.

You, L., *et al*., 2018. Spectral element method for dynamic response of transversely isotropic asphalt pavement under impact load. *Road Materials and Pavement Design*, 19 (1), 223–238. doi:10.1080/14680629.2016.1230513

Zhang, Z., *et al*., 2015. Damage of surface layer of asphalt concrete pavement under launching impact load. *Engineering Mechanics*, 32 (10), 161–168. doi:10.3901/JME.2015.24.161

Zhang, Q., *et al*., 2019. Study of automated top-coal caving in extra-thick coal seams using the continuum-discontinuum element method. *International Journal of Rock Mechanics and Mining Sciences*, 122 (2019), 104033. doi:10.1016/j.ijrmms.2019.04.019

Zhang, Q., *et al*., 2020a. Investigation of concrete pavement cracking under multi-head impact loading via the continuum-discontinuum element method. *International Journal of Impact Engineering*, 135 (2020), 103410. doi:10.1016/j.ijimpeng.2019.103410

Zhang, W., Chen, S., and Liu, Y, 2017. Effect of weight and drop height of hammer on the flexural impact performance of fiber-reinforced concrete. *Construction and Building Materials*, 140 (2017), 31–35.

Zhang, X., Hu, Y., and Lin, Y, 2020b. The influence of highway on local economy: Evidence from China's Yangtze River Delta region. *Journal of Transport Geography*, 82 (2020), 102600. doi:10.1016/j.jtrangeo.2019.102600

Zhao, L., and Jiang, Y, 2018. A study on launch site ground of vehicle-mounted missile based on elastic layer theory. *Advances in Mechanical Engineering*, 10 (10), 168781401880732–10. doi:10.1177/1687814018807322

Zhen, B., Xu, J., and Sun, J, 2020. Analytical solutions for steady state responses of an infinite Euler-Bernoulli beam on a nonlinear viscoelastic foundation subjected to a harmonic moving load. *Journal of Sound and Vibration*, 476 (2020), 115271. doi:10.1016/j.jsv.2020.115271

Zhou, X., *et al*., 2014. Quantitative trait loci associated with major fatty acid components in Soybean. *Acta Agronomica Sinica*, 40 (10), 1595–1603. doi:10.3724/SP.J.1006.2014.01595